

**Optimization of coherent lidar performance using graded-reflectance
transmitter resonator optics in the low equivalent Fresnel number regime**

David M. Tratt

Jet Propulsion Laboratory
California Institute of Technology
4800 Oak Grove Drive
Pasadena, CA 91109

Mark S. Hevelers

Aculight Corp.
40 Lake Bellevue
Bellevue, WA 98005

ABSTRACT

Using a diffractive eigenmode treatment to model the laser output we show that graded-reflectance resonator optics offer significant efficiency benefits over conventional hard-edge coupled unstable resonators in the context of coherent detection lidar applications. Extending previous work pertinent to the high equivalent Fresnel number regime, we have modelled the optimum performance of a notional super-Gaussian coupled cavity as a function of the key resonator parameters in the low equivalent Fresnel number (<3) regime. The findings from this study are applicable to the design of coherent lidar transmitters operated within this regime.

1. Introduction

The overall efficiency of a coherent detection lidar system is contingent on numerous empirical factors, not the least of which are the beam quality and output energy of the transmitter laser. Previously, it has been shown how both of these quantities can be influenced by the nature of the cavity optics themselves, i.e., by the use of graded reflectance output couplers^{1,2}. For a number of years the use of graded-reflectance resonator optics has been advocated as a means of improving the spatial properties of the laser output, based on the putative ability of such optics to impose a well-defined transverse profile on the output beam^{3,4}. While this approach has yielded much useful insight into the question at hand, it nevertheless only has validity in the case where N_{eq} is sufficiently large that the laser mode can justifiably be described using the geometric limit approximation and thus has limited utility. Since the assumption of mode profile determinism by the cavity optics breaks down at low N_{eq} as the reflectivity gradient increases, an accurate rendering of this issue requires a full diffractive eigenmode treatment of the resonator output.

In the initial study¹ a figure-of-merit Q was defined which included both the resonator energy extraction efficiency (expressed in terms of the modal cavity filling factor Q_v) and the far-field beam brightness (expressed in terms of the antenna efficiency η) to yield an indication of the power transmission efficiency into the far-field:

$$Q = \eta Q_v . \quad (1)$$

We shall use this figure-of-merit in the present study also in order to quantify the performance of various resonator structures and their concomitant suitability for coherent lidar applications.

2. Transmitter Resonator Model

For the purposes of the present study the family of functions known as *super-Gaussians* has once again been chosen to describe the radial variation of the coupled reflectivity $R(r)$:

$$R(r) = R_0 \exp[-2(r/w_m)^n], \quad (2)$$

where R_0 is the on-axis reflectance, r the radial ordinate, w_m is the C^2 radius of the reflectance profile, and n is the super-Gaussian order. Also in common with the previous studies, we assume a positive-branch (Cassegrain) confocal unstable resonator. The fundamental transverse mode field $u_m(r)$ of the resonator is computed by numerical solution of the cavity eigenfunction⁵ for selected values of the cavity magnification M and equivalent Fresnel number N_{eq} :

$$\gamma u_m(\xi) = \frac{4\pi i M N_{eq} \sqrt{R_0}}{M^2 - 1} \int_0^\infty \exp\left[-\frac{2inMN_{eq}}{M^2 - 1} \left(M\xi_0^2 + \frac{\xi^2}{M}\right)\right] \exp(-\xi_0^n) u_m(\xi_0) J_0\left(\frac{4\pi M N_{eq} \xi \xi_0}{M^2 - 1}\right) \xi_0 d\xi_0 \quad (3)$$

where γ is the eigenvalue of the fundamental mode, J_0 is the ordinal y Bessel function of zeroth order, and ξ, ξ_0 are normalized radial coordinates. The equivalent Fresnel number is given by⁵:

$$N_{eq} = \left(\frac{M^2 - 1}{2M}\right) \frac{w_m^2}{B\lambda}, \quad (4)$$

in which λ is the laser wavelength and B is the effective cavity round-trip excursion distance.

The resonator energy extraction efficiency is frequently regarded as proportional to the degree of overlap between the cavity mode and the available, gain volume; a quantity often referred to as the cavity filling factor. Since we are assuming a confocal resonator, and therefore collimated output, the cavity filling factor, while strictly speaking a three-dimensional property, may be reduced to a two-dimensional integration. Thus Q_v may be described in terms of the

ratio of the mode area of the laser to that of a plane wave ($u_m = 1 \forall r < b$, where b is the limiting aperture radius of the lidar transmitter laser)⁶:

$$Q_v = \frac{\int_0^b |u_m(r)|^2 d^2r}{\int_0^b d^2r}, \quad (5)$$

Much has been written concerning the optimum intracavity aperture for a given laser device. The central issue here is the trade-off between maximal utilization of the available gain volume as set against the detrimental effect of diffraction induced by interference with the laser mode by elements of its physical environs (e.g., containment vessel, discharge electrodes, laser rod walls, finite optics boundaries, etc.). For the case of a Gaussian profiled reflector ($n = 2$) analysis has shown⁶ that a reasonable balance prevails for an output beam truncation $b/w_0 \approx 1.4$. We may expect this figure to converge to unity as higher order super-Gaussian profiled optics are considered, (Silvestri, et al. state as a “rule of thumb” that vignetting of the beam should not be allowed to exceed the 5% of peak power level⁴). However, it should also be noted that practical laser systems rarely evince useful gain at the periphery of the excited medium, so that it should be considered inappropriate to equate the upper integration limit of Eq. (5) to the actual physical extent of the laser gain medium. A more accurate measure of gain volume utilization can perhaps be estimated by considering the overlap between the laser mode and the usable gain volume (to which we assign a radius b ; the upper limit of our integration). Theoretical and experimental analysis of a Gaussian beam laser system⁷ has demonstrated that optimum performance obtains for $b/w_0 \approx 1$. Since this result can be expected to pertain to an even greater degree for the more compact super-Gaussian modes ($n > 2$), we have adopted it for each implementation of Eq. (5) which was necessary for the present study.

3. Coherent Lidar Model

The coherent lidar transceiver configuration is assumed to comprise a coaxial matched-pupil geometry and the backpropagated local oscillator formalism is used to simulate the coherent mixing process⁸, so that the antenna efficiency η for a nominally diffuse aerosol target adopts the form⁹:

$$\eta = \frac{T_T \lambda^2 z^2}{A_T} \frac{\left| \int_0^\infty U_T(\rho) U_L^*(\rho) d^2 \rho \right|^2}{\left[\int_0^a |U_T(r)|^2 d^2 r \int_0^a |U_L(r)|^2 d^2 r \right]}, \quad (6)$$

where z is the range to the target, U_x is the complex transverse field descriptor, ρ is the radial ordinate at the target plane, and A_T is the pupil area (πa^2). The subscripts connote the transmitter beam ('T') and the backpropagated local oscillator (L) and T_T is the transmit beam pupil transmission function, given by:

$$T_T = \frac{\int_0^a |U_T(r)|^2 d^2 r}{\int_0^\infty |U_T(r)|^2 d^2 r}, \quad (7)$$

since we are assuming radially symmetric profiles concentric with the transceiver pupil (radius a). Substituting this identity into Eq. (7) and accounting for the radial symmetry property we thus obtain:

$$\eta = \left(\frac{\lambda z}{a} \right)^2 \frac{\left| \int_0^\infty U_T(\rho) U_L^*(\rho) 2\rho d\rho \right|^2}{\left[\int_0^\infty |U_T(r)|^2 2\pi r dr \right] \left[\int_0^a |U_L(r)|^2 2\pi r dr \right]}, \quad (8)$$

in which:

$$U_T(r) = u_m(r) [1-R(r)]^{1/2}. \quad (9)$$

The local oscillator field $U_L(r)$ is assumed to be flat-phase Gaussian at the transceiver pupil plane with an e^{-2} intensity radius of w_L and a truncation parameter at the pupil of $a/w_L = 0.84$. This local oscillator field specification is optimum for arbitrary transmit beam profile, as was indicated empirically in a previous study¹ and later demonstrated explicitly by Frehlich¹⁰.

The far-field beam irradiances $U_x(\rho)$ are computed by means of the free-space Fraunhofer diffraction relation:

$$U_x(\rho) = \frac{2\pi i}{z\lambda} \exp\left(\frac{-i\pi\rho^2}{z\lambda}\right) \int_0^a r U_x(r) J_0\left(\frac{2\pi r\rho}{z\lambda}\right) dr. \quad (10)$$

Here, w_0 is the transmitter beam radius, defined as³:

$$W = w_m(M^n - 1)^{1/n}. \quad (11)$$

For each selected resonator configuration the transmitter beam truncation parameter a/w_0 is incremented and Eq. (8) evaluated until an optimum operating point is identified.

4. Parametric Behavior of Lowest Order Resonator Eigenmode

For this study we have selected values of the cavity magnification $M = 1.5, 2.0, 2.5$ (the condition $M = 2$ is frequently specified because it maximizes N_{eq} for a given resonator configuration¹¹) and values of the equivalent Fresnel number $N_{eq} = 0.5, 1.5, 2.5$. These half-integral N_{eq} values correspond to the optimum transverse mode discrimination design points for a radially symmetric hard-edge coupled unstable resonator¹² and were selected in order to directly compare these resonator structures with their super-Gaussian coupled counterparts. (At least for low order super-Gaussian reflectors this recommended restriction on the value of N_{eq} does not apply⁵.)

For each combination of these parameters the super-Gaussian order n was incremented between 2 and 20 and the resultant fundamental resonator mode field components extracted by solving Eq. (3). For illustrative purposes, we reproduce the radial variation of mode intensity and residual phase as a function of n for the three $M = 2$ cases in Figures 1-3. We may note that for $n = 2$ there is very little perturbation of the geometric transverse mode profile by diffraction effects and the phasefront is virtually flat across its profile. At which point the diffraction-induced beam structure becomes significant is very much dependent on N_{eq} . For the case where $N_{eq} = 0.5$ the geometric solution is invalid beyond $n = 2$ (see Fig. 1), whereas the geometric limit remains a reasonable approximation out to $n = 6$ for $N_{eq} = 1.5$ (Fig. 2) and out to $n = 8$ for $N_{eq} = 2.5$ (Fig. 3). (We shall see later in our discussion of Fig. 15 how fundamental these particular observations are in relation to overall lidar efficiency.) As $N_{eq} \rightarrow \infty$ the solution of Eq.(3) thus converges to the geometric limit; the situation which was represented in the previous study². Although in all instances the wavefront phase begins to degrade at $n > 2$, the degree of deterioration remains relatively small until the extreme wings of the intensity distribution are reached. Phasefront degradation therefore contributes only marginally to that of the overall system performance. We will see in the following section how these behavioral trends correlate closely with the theoretical coherent lidar performance.

For comparison purposes we also show the mode intensity profile and residual phase for the corresponding hard-edge coupled resonators in Figure 4. The lack of gain volume utilization efficiency is immediately apparent in the upper panel of Fig. 4. This, combined with the considerable irregularities in both intensity and phase, are the principle origins of the poor

coherent lidar performance predicted for these cavity architectures when compared to their super-Gaussian coupled counterparts (see Figs. 6-14).

Dependences of the zero-order eigenmode feedback ratio on n for the $M = 2$ case and for the salient values of N_{eq} are shown in **Figure 5**. Note that as N_{eq} increases, the feedback ratio tends to converge toward the value prevailing at the geometric optics limit.

5. Parametric Behavior of Coherent Lidar Performance

To assess dependence of the coherent lidar performance on the coupler reflectance profile we track η , $a/w_0|_{opt}$, Q_v , and Q as a function of n and R_0 for each of the cavity configurations identified in the previous section. By setting unity R_0 and allowing, $n \rightarrow \infty$ we may also model the behavior of the equivalent hard-edged coupler for each case. Figures 6-14 contain the results of this parametric study for all nine combinations of M and N_{eq} considered here, with the equivalent hard-edged coupler case being represented in each instance by the horizontal broken line (HEC). The major difference between the present results and those reported for the geometrically obtained laser modes in Ref. 2, is that we now observe a finite- n optimum operating point (as opposed to asymptotically increasing performance metrics²) as diffraction effects become increasingly important at larger values of n . In each of these figures it is apparent that the principle contribution to Q originates from the behavior of Q_v rather than the more slowly varying η . In general we may note from these displays that the figure-of-merit increases with N_{eq} , while decreasing with M . This result essentially reflects the weaker influence of diffraction processes at higher N_{eq} . Note that because the laser intracavity aperture is now decoupled from the lidar pupil the extraction efficiency Q_v is independent of R . (cf.

Ref. 2), so that only a single set of data are now required to describe this property for a given resonator case.

The exact value of n that yields the optimum operating point is a non-trivial function of M , R_0 , and N_{eq} , but in the case of $N_{eq} = 1.5$ (Figures 9-11), a well-defined optimum can be inferred to lie near $n = 6$, ostensibly independent of M . For $N_{eq} = 2.5$ (Figures 12-14) the optimum operating point is somewhat broader and more sensitive to M , migrating from $n = 7$ at $M = 2.5$ to $n = 8$ at $M \leq 2.0$; the optimum Q values approach those previously computed for the $N_{eq} \rightarrow \infty$ limit². However, the $N_{eq} = 0.5$ case (Figures 6-8) exhibits a fundamentally different character in that the lidar performance metrics decline asymptotically with n and do not reach a stationary point. Another significant observation we may make is that although the absolute performance of the lidar system is affected by R_0 (except in the $N_{eq} = 0.5$ case, where Figs. 6-8d evince no R_0 dependence whatsoever), the optimum value of n is essentially independent of R_0 . This is a useful result in that it provides an unequivocal starting point for designing a super-Gaussian coupler in a system with known M and N_{eq} . Note that in all cases examined here the super-Gaussian coupled resonator far outperforms its hard-edge coupled equivalent, although it must be emphasized that these results obtain for *low equivalent Fresnel number cavities*; such impressive performance gains with super-Gaussian optics are not observed in practical systems of moderate-to-high (>5) equivalent Fresnel number^{13,14}.

It has been noted¹² that excellent transverse mode discrimination is afforded by operation in the vicinity of $N_{eq} = 0.5$ (at least for hard-edge coupled resonators). However, it is clear from comparison of the above results that such a choice would yield poor lidar performance.

Nevertheless, it is possible to conceive of the circumstance where a low SNR lidar application could trade performance for optimum output stability, in which case we are able to state that a Gaussian-profiled ($n = 2$) coupler would suffice for optimum performance; nothing is gained by the use of super-Gaussian optics, as can be discerned from Figs. 6-8.

Figure 15 summarizes the above findings. The form of the fitted curve indicates asymptotic behavior of the computed optimum n as a function of N_{eq} . For $N_{eq} < 2.5$ the optimum n was found to be essentially independent of the cavity magnification M over the range investigated during the current study. The vertical bar at $N_{eq} = 2.5$ represents a range of values of n_{opt} and denotes the point at which the onset of significant dependence on M is observed.

6. Conclusion

This study has provided further evidence that graded-reflectance output couplers can be employed to significantly enhance the performance of unstable resonator laser transmitters in coherent lidar applications. The unloaded cavity results presented here show significant dependence of the optimum operating point on the salient unstable resonator parameters: n , M , R_0 , and N_{eq} . These generalized findings constitute a useful indicator of the likely benefit to be expected on converting a conventional hard-edge coupled unstable resonator lidar transmitter to a graded-reflectivity coupler configuration. However, application of this formalism to analyse the performance envelope of a given system-specific resonator architecture should ultimately incorporate factors relating to the laser medium itself, since the dynamics of the gain medium can drastically modify the resonator eigenmode structure from the empty cavity case in certain circumstances^{15,16}.

Acknowledgements

Portions of this work were conducted at the Jet Propulsion Laboratory (JPL), California Institute of Technology (Caltech), under contract with the National Aeronautics and Space Administration, using computing resources provided by the JPL/Caltech Supercomputing Project.

References

1. D. M. Tratt and R. T. Menzies, "Unstable resonator antenna properties in coherent lidar applications: a comparative study," *Appl. Opt.*, 27, 3645-3649 (1988).
2. D. M. Tratt, "Optimizing coherent lidar performance with graded-reflectance laser resonator optics," *Appl. Opt.*, 31, 4233-4239 (1992).
3. S. De Silvestri, P. Laporta, V. Magni, and O. Svelte, "Solid-state laser unstable resonators with tapered reflectivity mirrors: The super-Gaussian approach," *IEEE J. Quantum Electron.*, 24, 1172-1177 (1988).
4. S. De Silvestri, V. Magni, O. Svelte, and G. Valentini, "Lasers with super-Gaussian mirrors," *IEEE J. Quantum Electron.*, 26, 1500-1509 (1990).
5. M. S. Bowers, "Diffractive analysis of unstable optical resonators with super-Gaussian mirrors," *Opt. Lett.*, 17, 1319-1321 (1992).
6. A. Parent, N. McCarthy, and P. Lavigne, "Effects of hard apertures on mode properties of resonators with Gaussian reflectivity mirrors," *IEEE J. Quantum Electron.*, **QE-23**, 222-228 (1987),
7. D. G. Hall, "Optimum mode size criterion for low-gain lasers," *Appl. Opt.*, 20, 1579-1583 (1981).
8. A. E. Siegman, "The antenna properties of optical heterodyne receivers," *Appl. Opt.*, 5, 1588-1594 (1966).
9. B. J. Rye, "Primary aberration contribution to incoherent back scatter heterodyne lidar returns," *Appl. Opt.*, 21, 839-844 (1982).
10. R. G. Frehlich, "Optimal local oscillator field for a monostatic coherent laser-radar with a circular aperture," *Appl. Opt.*, 32, 4569-4577 (1993).

11. A. E. Siegman, "Stabilizing output with unstable resonators," *Laser Focus*, 7, May 1971, 42-47.
12. A. E. Siegman and H. Y. Miller, "Unstable optical resonator loss calculations using the Prony method," *Appl. Opt.*, 9, 2729-2736 (1970).
13. S. De Silvestri, P. Laporta, V. Magni, G. Valentini, and G. Cerullo, "Comparative analysis of Nd:YAG unstable resonators with super-Gaussian variable reflectance mirrors," *Opt. Commun.*, 77, 179-184 (1990).
14. S. E. Kovalenko, V. Losev, and M. R. Perrone, "Super-Gaussian resonators for long-pulse XeCl lasers," *Appl. Opt.*, 33, 4082-4086 (1994).
15. M. S. Bowers and S. E. Moody, "Numerical solution of the exact cavity equations of motion for an unstable optical resonator," *Appl. Opt.*, 29, 3905-3915 (1990).
16. T. R. Ferguson, "Unstable resonators with distributed saturable gain and nonuniform reflectivity outcouplers in the geometric optics limit," *Appl. Opt.*, 31, 7551-7556 (1992).

Figure Captions

- Figure 1. Dependence of $M = 2$ unstable cavity fundamental mode intensity (upper) and phase (lower) on super-Gaussian order; $N_{eq} = 0.5$.
- Figure 2. Dependence of $M = 2$ unstable cavity fundamental mode intensity (upper) and phase (lower) on super-Gaussian order; $N_{eq} = 1.5$.
- Figure 3. Dependence of $M = 2$ unstable cavity fundamental mode intensity (upper) and phase (lower) on super-Gaussian order; $N_{eq} = 2.5$.
- Figure 4. Dependence of hard-edge coupled $M = 2$ unstable cavity fundamental mode intensity (above) and phase (below) for $N_{eq} = 0.5, 1.5$, and 2.5 .
- Figure 5. Feedback ratio of the lowest-loss transverse mode as a function of N_{eq} and for $M=2$.
- Figure 6. Dependence of (a) optimum antenna efficiency (η_{IEC} is off scale at -6.57 dB), (b) optimum truncation parameter, (c) cavity energy extraction, and (d) figure-of-merit on super-Gaussian order and on-axis reflectance of the lidar transmitter output coupler; $M = 1.5$ and $N_{eq} = 0.5$. The horizontal broken line represents the equivalent hard-edged coupler case.

Figure 7. Dependence of (a) optimum antenna efficiency, (b) optimum truncation parameter, (c) cavity energy extraction, and (d) figure-of-merit on super-Gaussian order and on-axis reflectance of the lidar transmitter output coupler; $M = 2.0$ and $N_{eq} = 0.5$. The horizontal broken line represents the equivalent hard-edged coupler case.

Figure 8. Dependence of (a) optimum antenna efficiency, (b) optimum truncation parameter, (c) cavity energy extraction, and (d) figure-of-merit on super-Gaussian order and on-axis reflectance of the lidar transmitter output coupler; $M = 2.5$ and $N_{eq} = 0.5$. The horizontal broken line represents the equivalent hard-edged coupler case.

Figure 9. Dependence of (a) optimum antenna efficiency (η_{HEC} is offscale at -6.73 dB), (b) optimum truncation parameter, (c) cavity energy extraction, and (d) figure-of-merit on super-Gaussian order and on-axis reflectance of the lidar transmitter output coupler; $M = 1.5$ and $N_{eq} = 1.5$. The horizontal broken line represents the equivalent hard-edged coupler case.

Figure 10. Dependence of (a) optimum antenna efficiency, (b) optimum truncation parameter, (c) cavity energy extraction, and (d) figure-of-merit on super-Gaussian order and on-axis reflectance of the lidar transmitter output coupler; $M = 2.0$ and $N_{eq} = 1.5$. The horizontal broken line represents the equivalent hard-edged coupler case.

Figure 11. Dependence of (a) optimum antenna efficiency, (b) optimum truncation parameter, (c) cavity energy extraction, and (d) figure-of-merit on super-Gaussian order and on-axis reflectance of the lidar transmitter output coupler; $M = 2.5$ and $N_{eq} = 1.5$. The horizontal broken line represents the equivalent hard-edged coupler case.

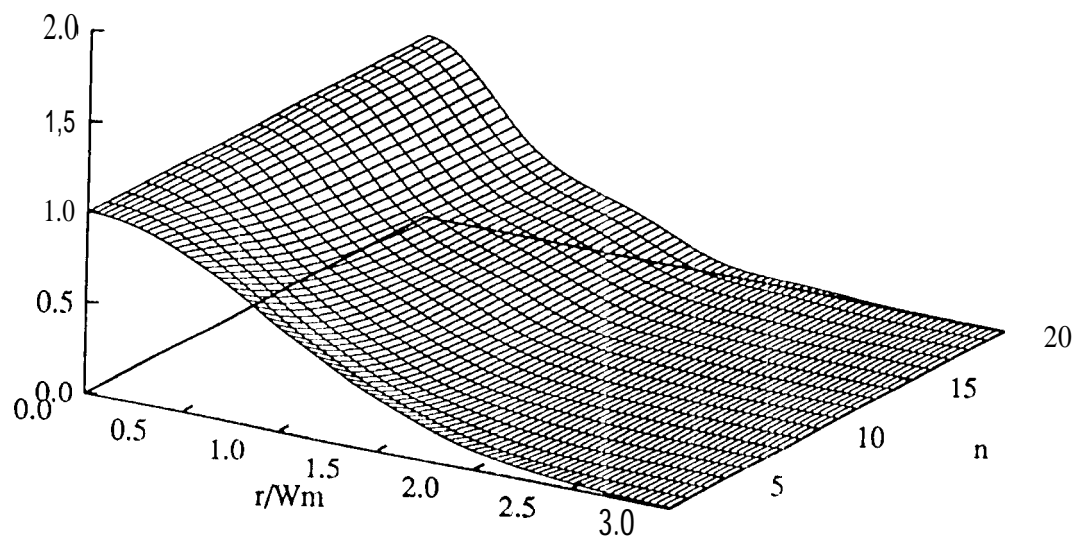
Figure 12. Dependence of (a) optimum antenna efficiency (η_{HFC} is offscale at -6.95 dB), (b) optimum truncation parameter, (c) cavity energy extraction, and (d) figure-of-merit on super-Gaussian order and on-axis reflectance of the lidar transmitter output coupler; $M = 1.5$ and $N_{eq} = 2.5$. The horizontal broken line represents the equivalent hard-edged coupler case.

Figure 13. Dependence of (a) optimum antenna efficiency, (b) optimum truncation parameter, (c) cavity energy extraction, and (d) figure-of-merit on super-Gaussian order and on-axis reflectance of the lidar transmitter output coupler; $M = 2.0$ and $N_{eq} = 2.5$. The horizontal broken line represents the equivalent hard-edged coupler case.

Figure 14. Dependence of (a) optimum antenna efficiency, (b) optimum truncation parameter, (c) cavity energy extraction, and (d) figure-of-merit on super-Gaussian order and on-axis reflectance of the lidar transmitter output coupler; $M = 2.5$ and $N_{eq} = 2.5$. The horizontal broken line represents the equivalent hard-edged coupler case.

Figure 15. Dependence of optimum super-Gaussian order on the resonator equivalent Fresnel number N_{eq} . The broken curve is provided only as a guide for the eye.

Mode Intensity (au.)



Residual Phase (rad.)

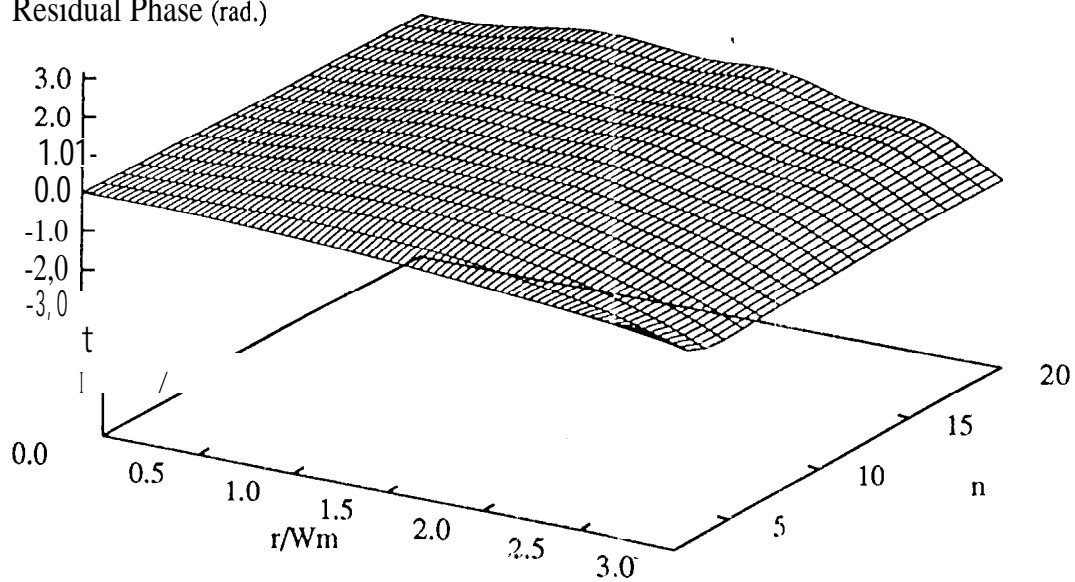
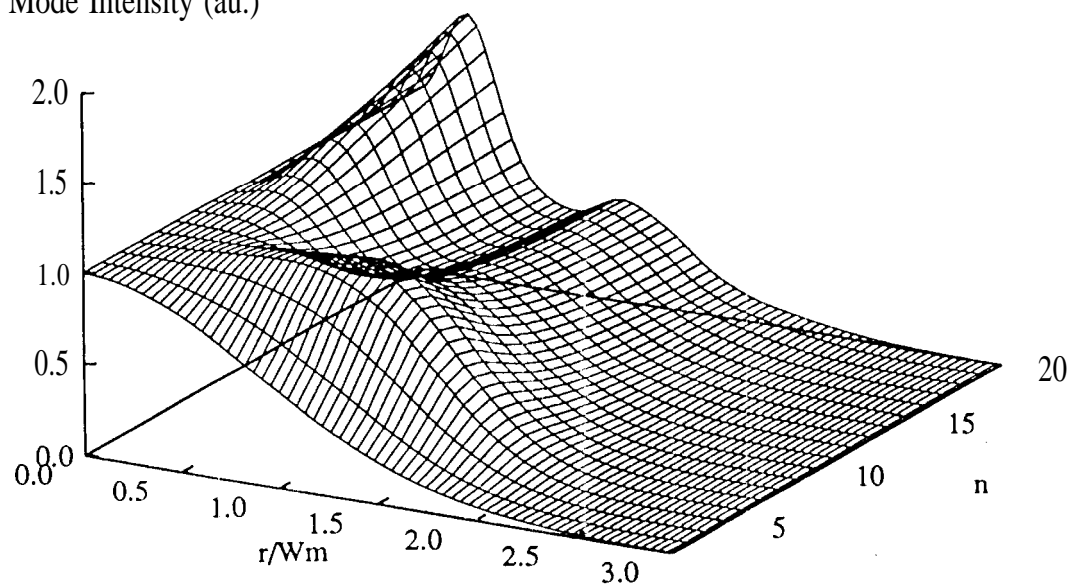


Fig. 1

Mode Intensity (au.)



Residual Phase (rad.)

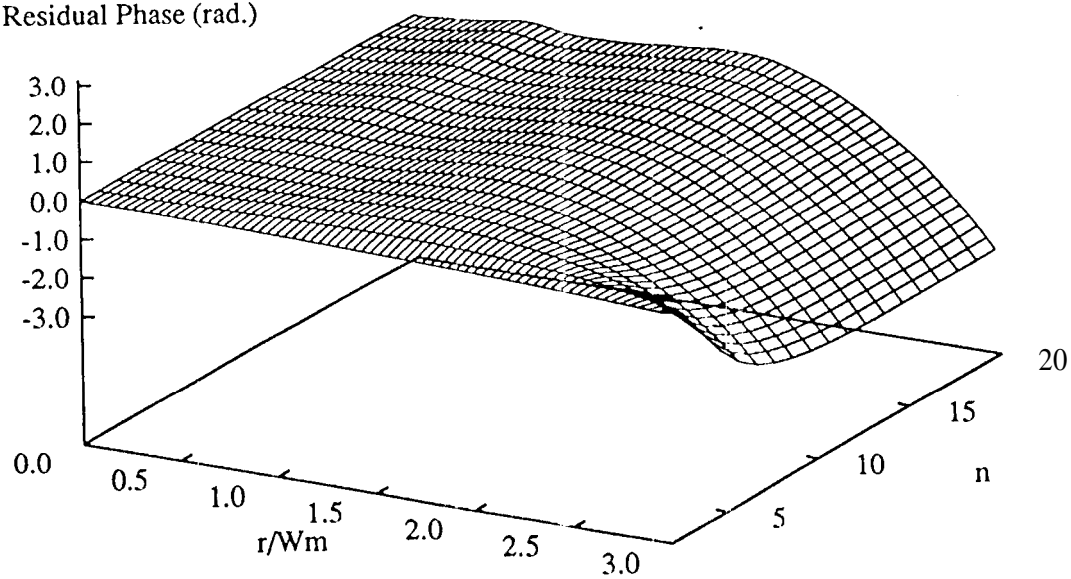
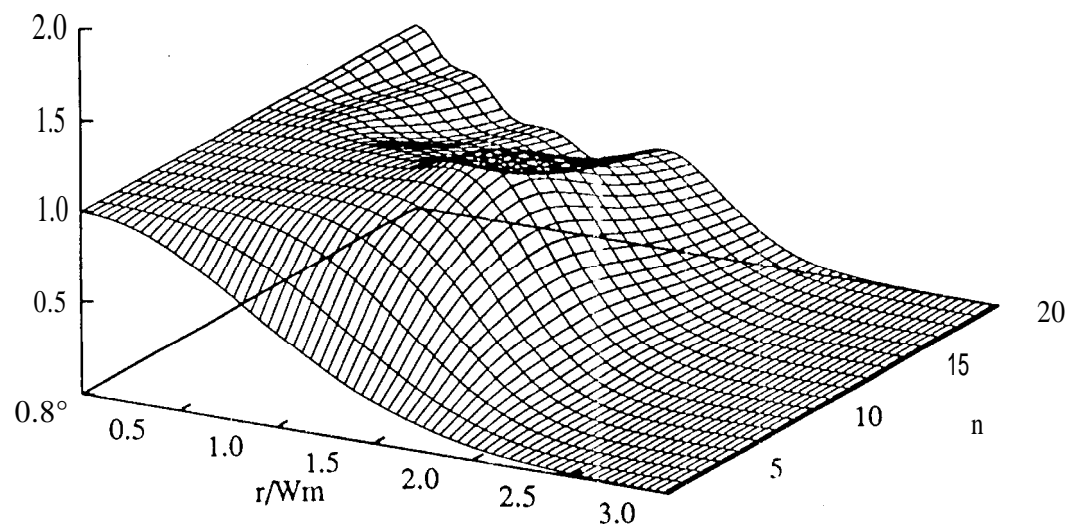


Fig.2

Mode Intensity (au.)



Residual Phase (rad.)

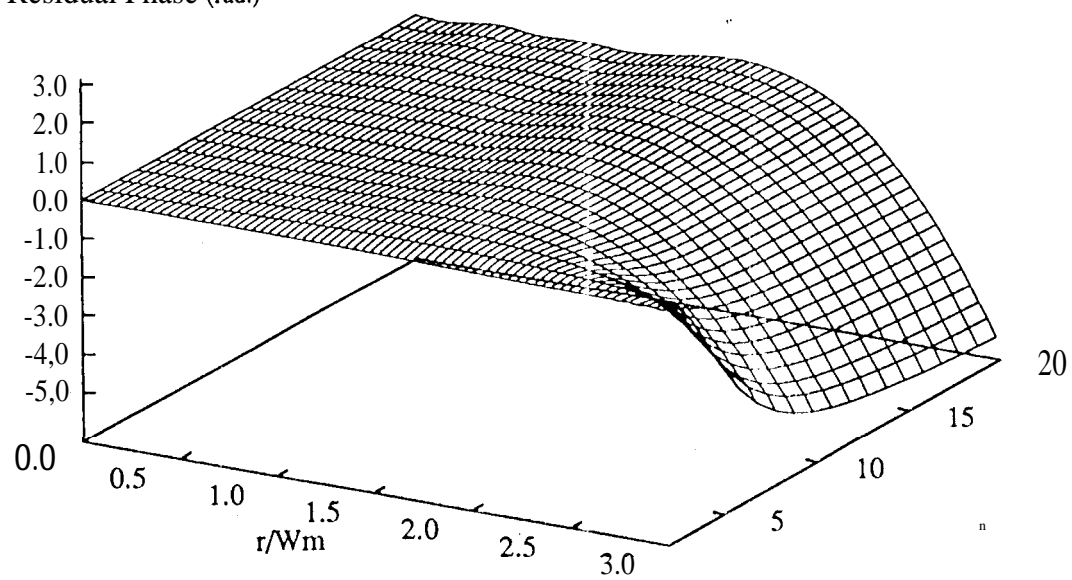


Fig. 3

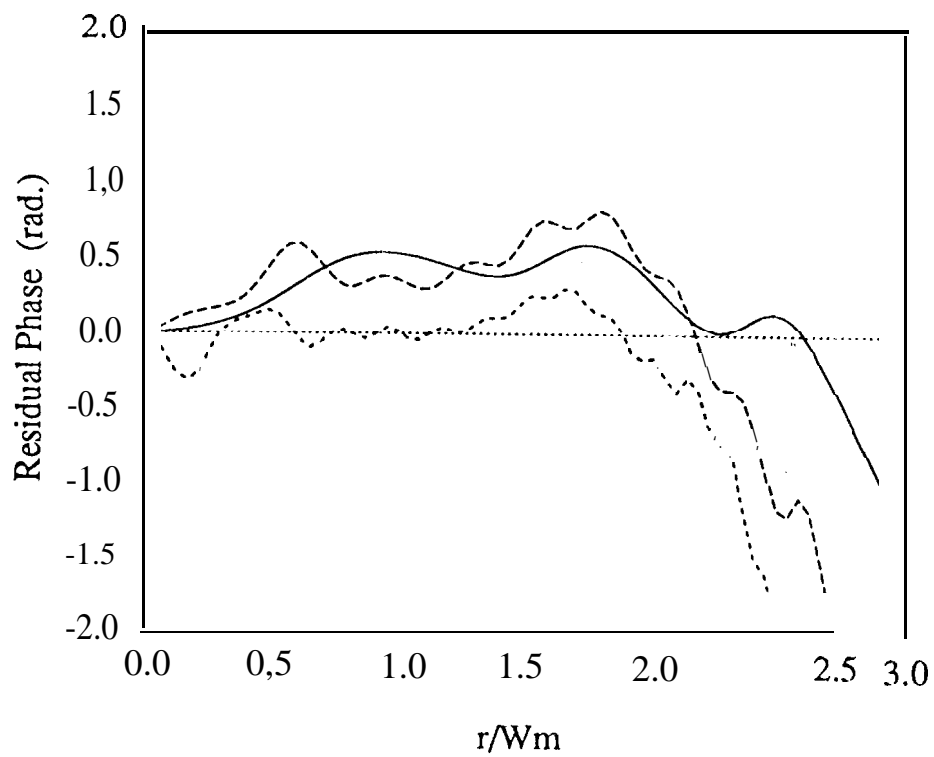
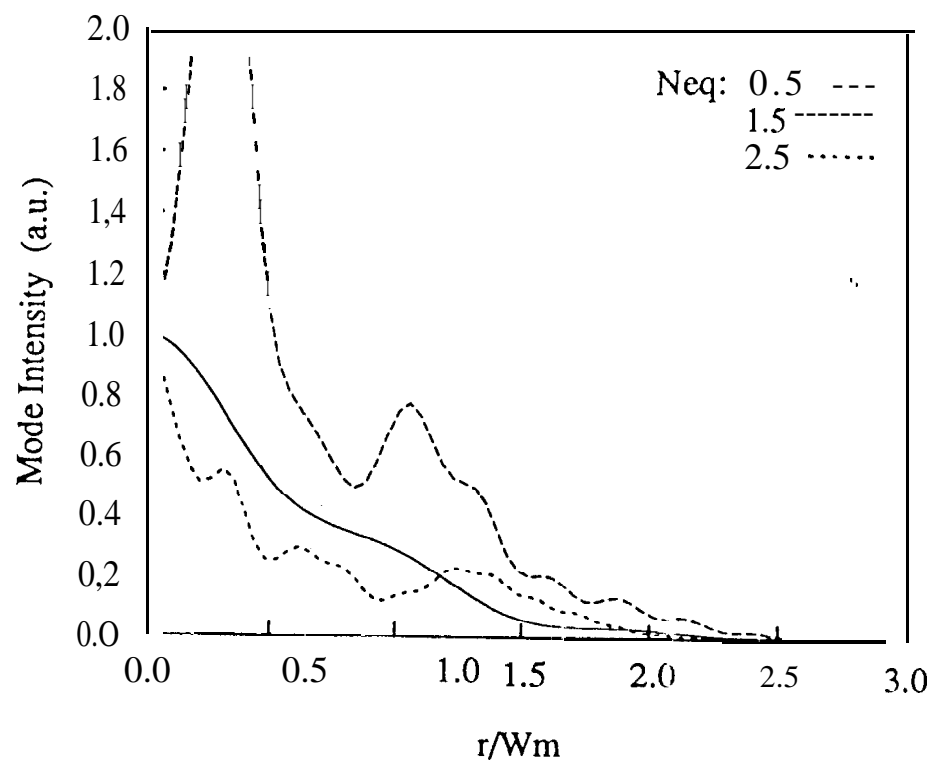


Fig. 4

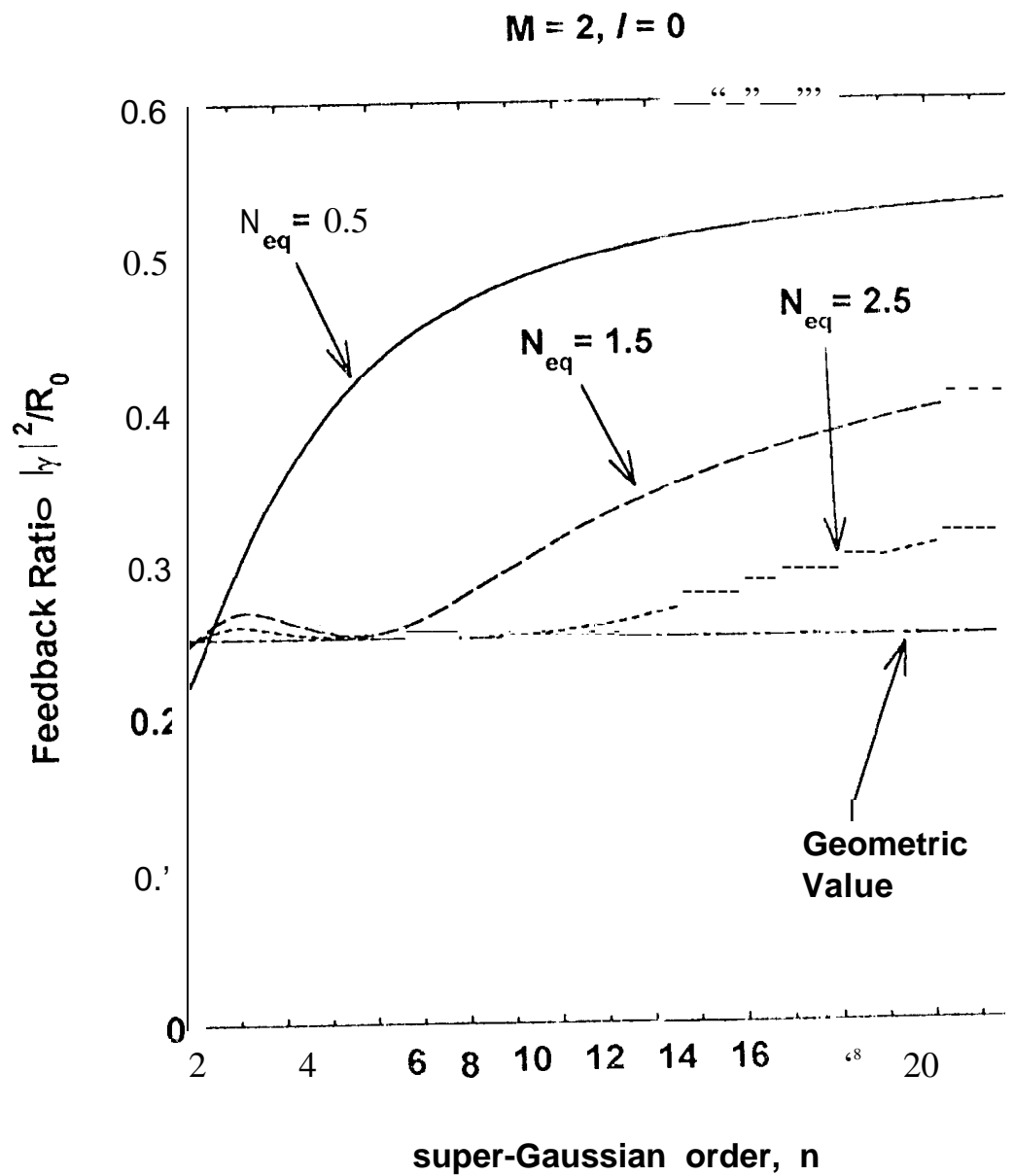


Fig. 5

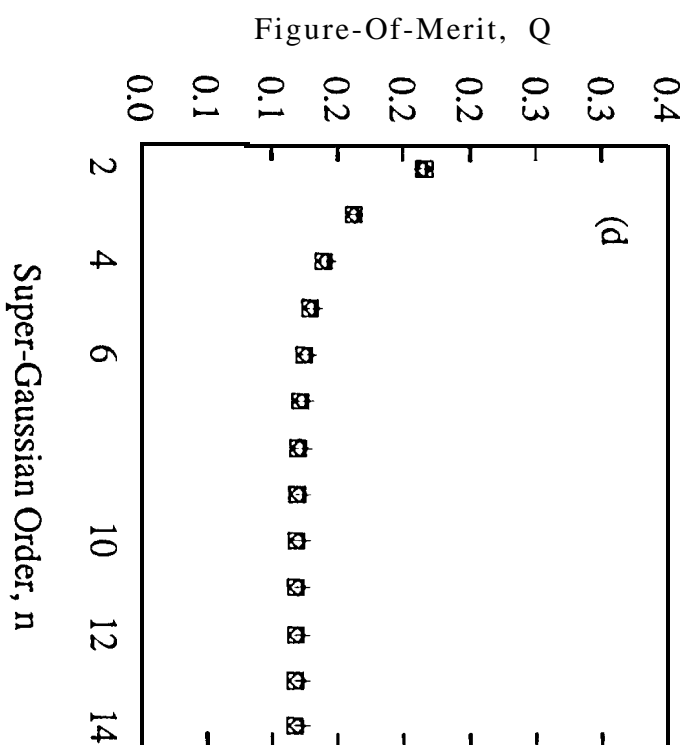
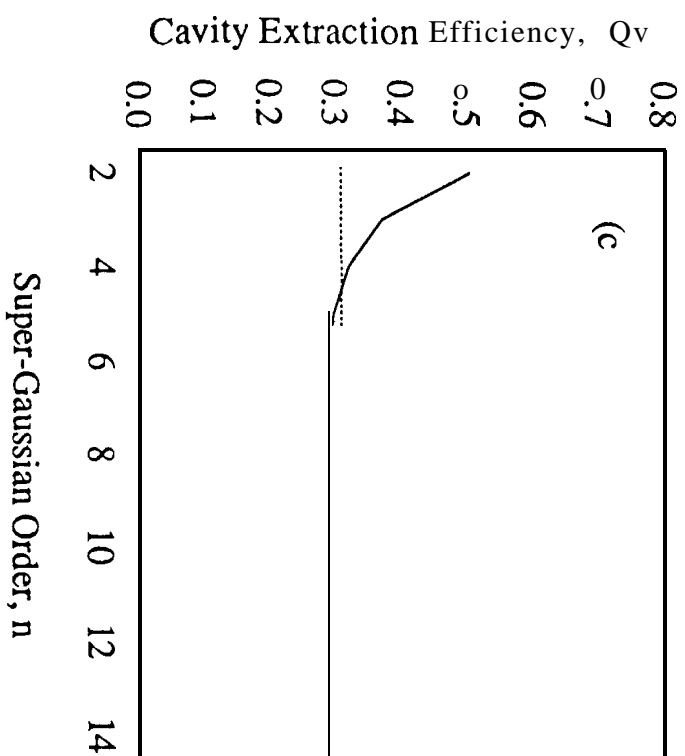
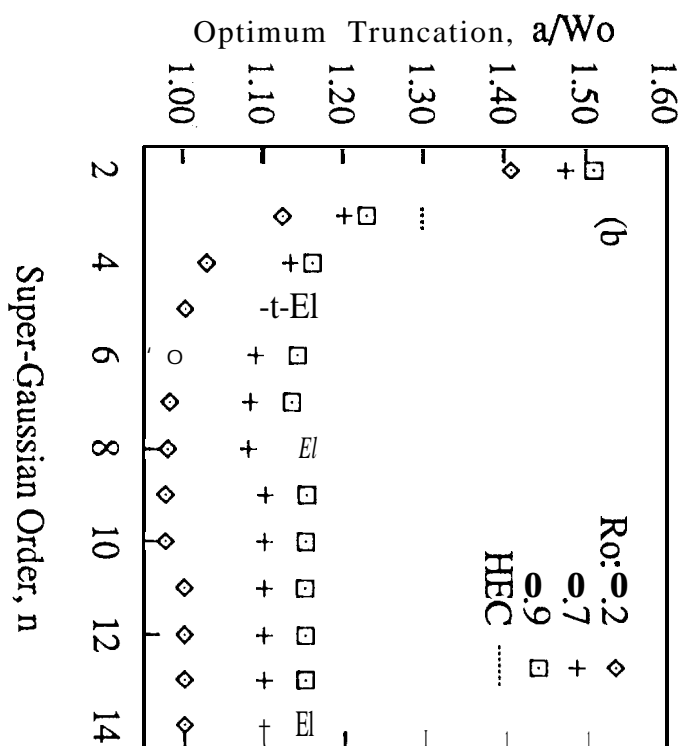
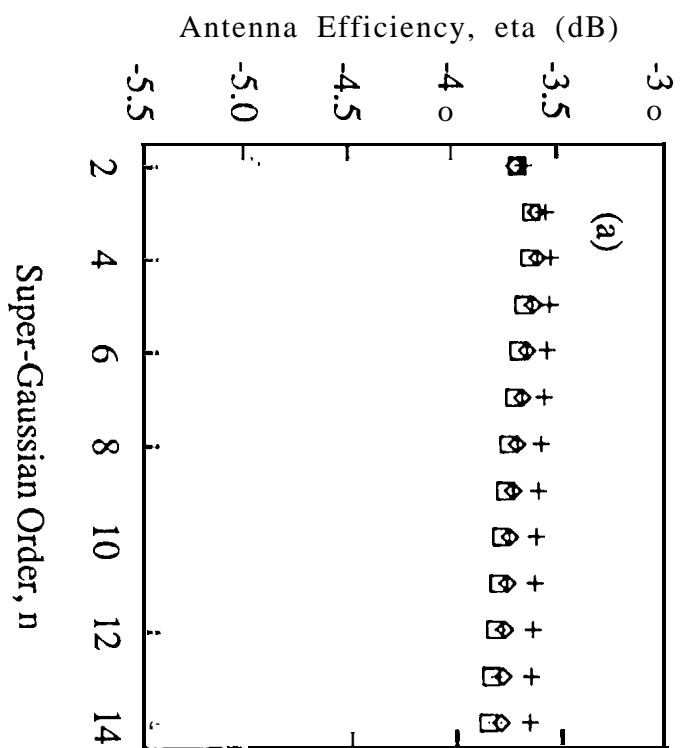


Fig. 6

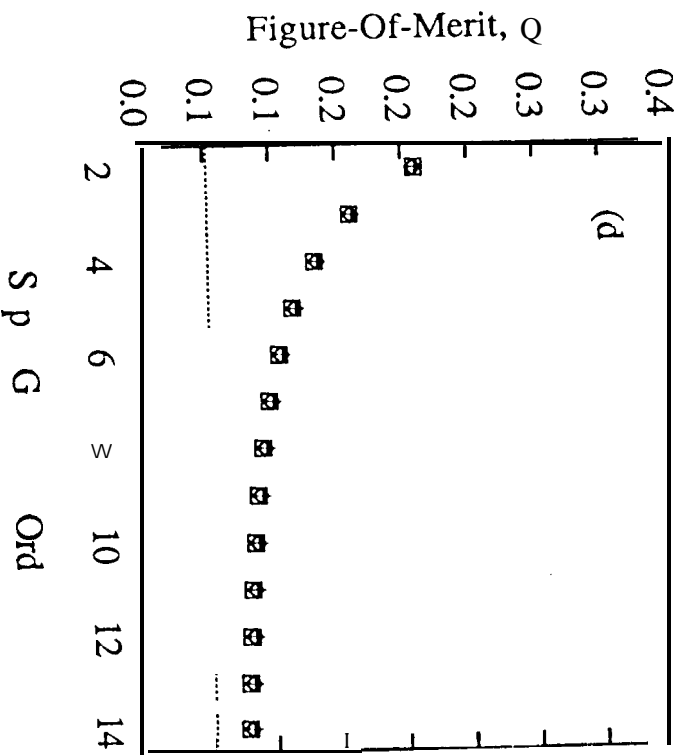
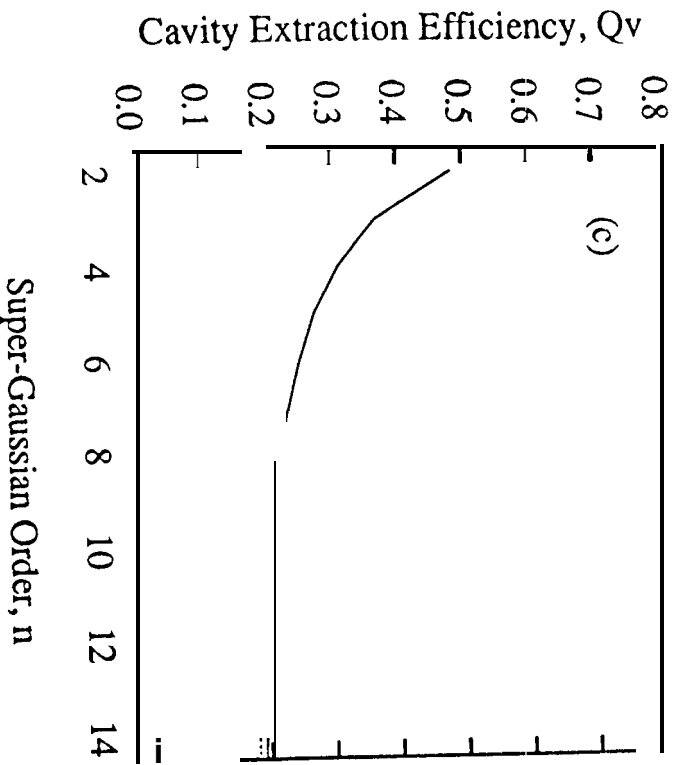
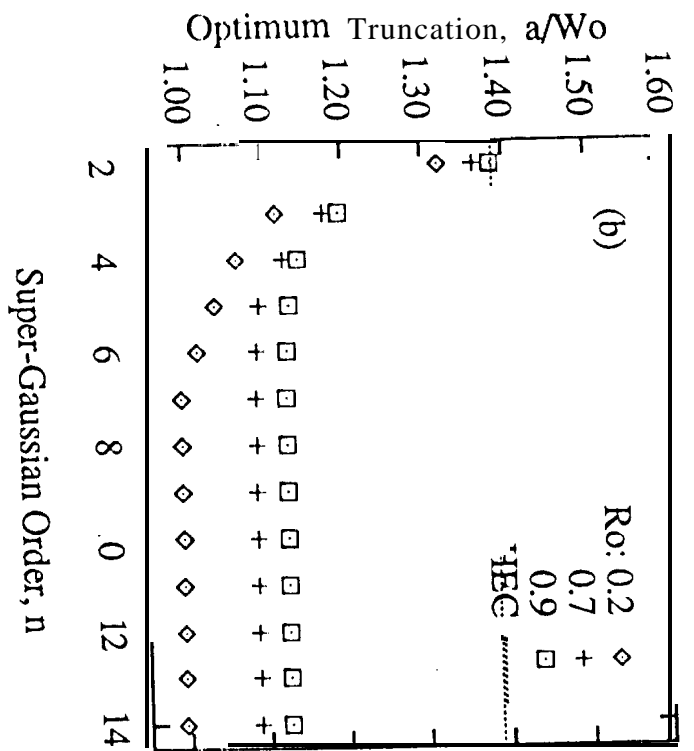
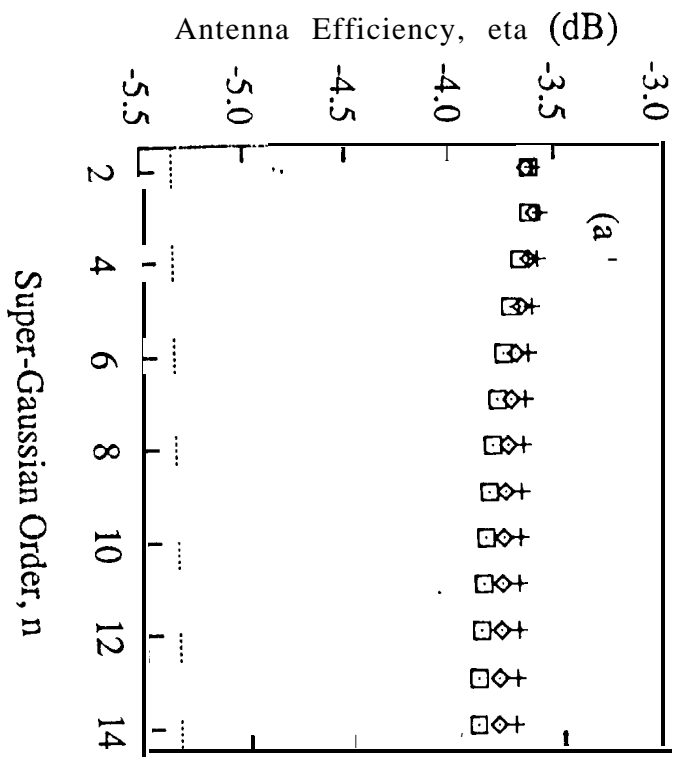


Fig. 7

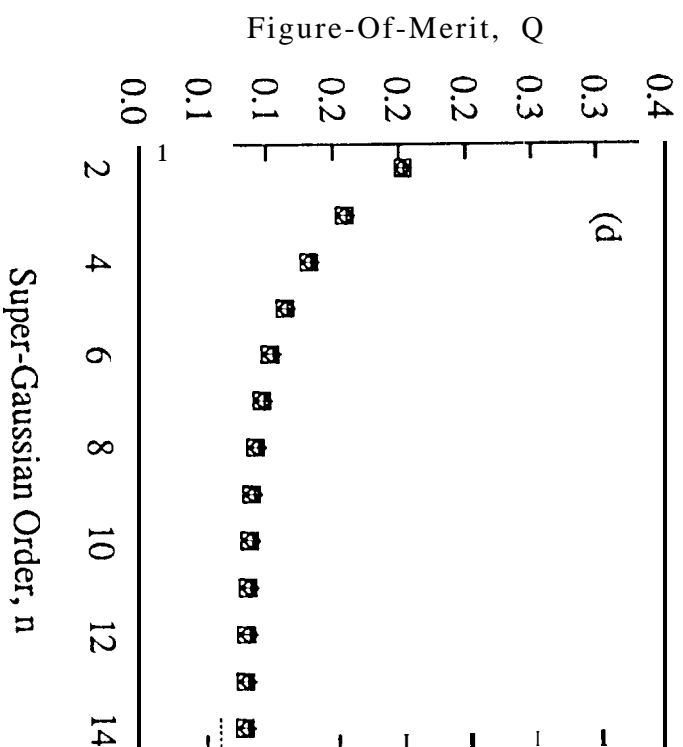
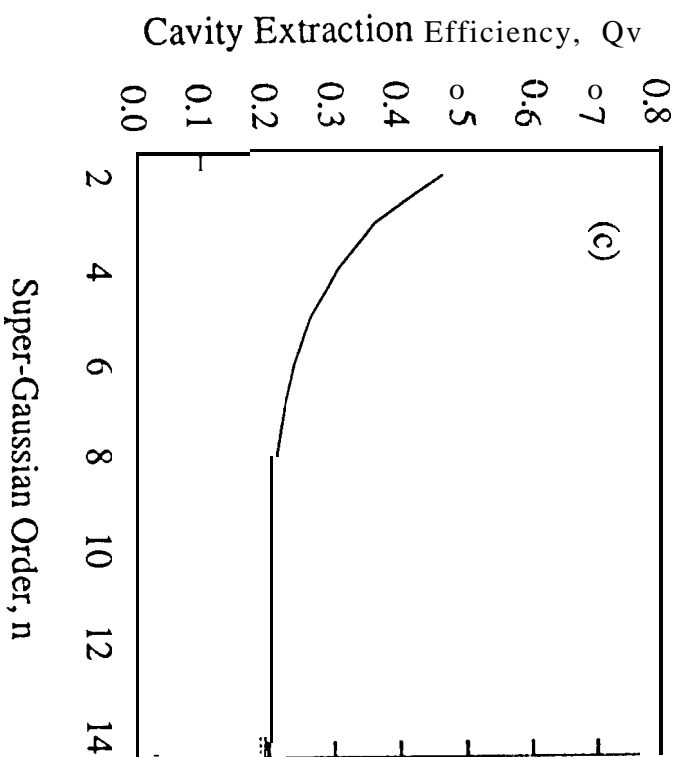
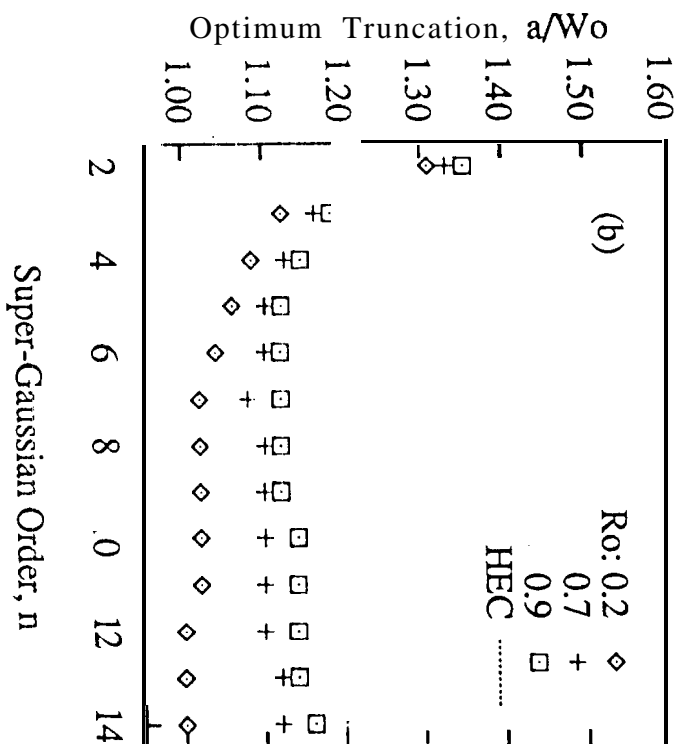
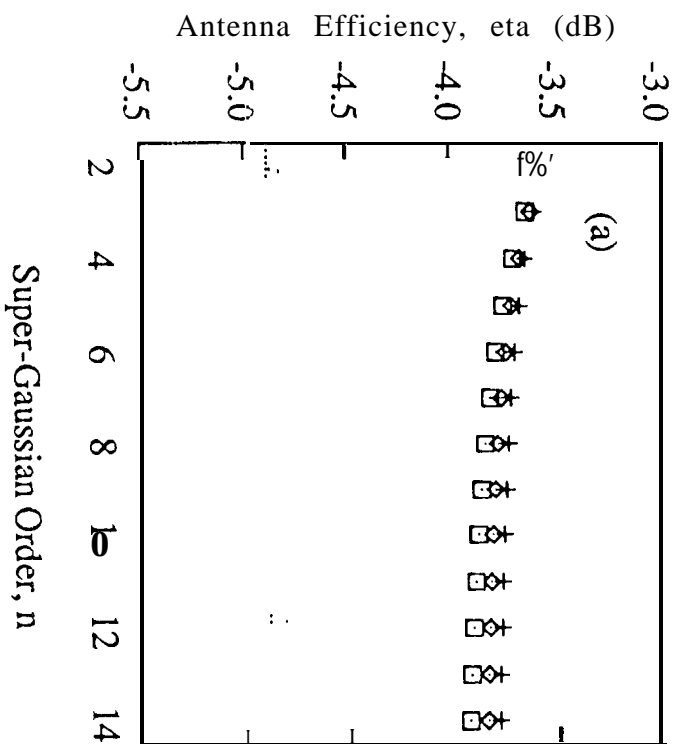


Fig. 8

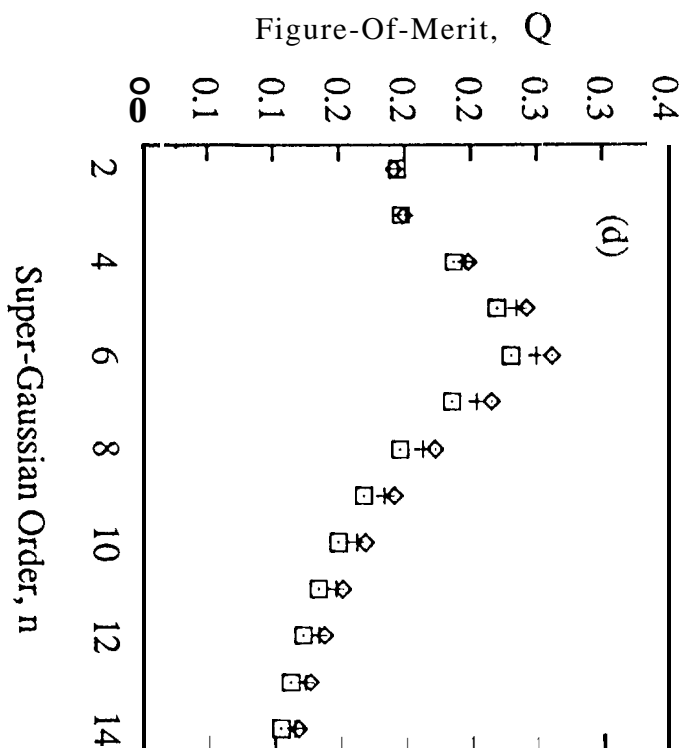
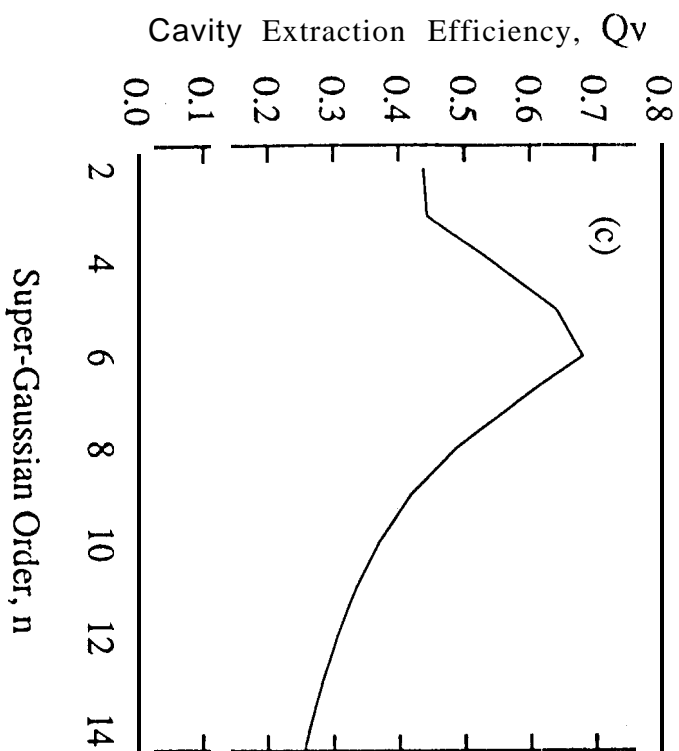
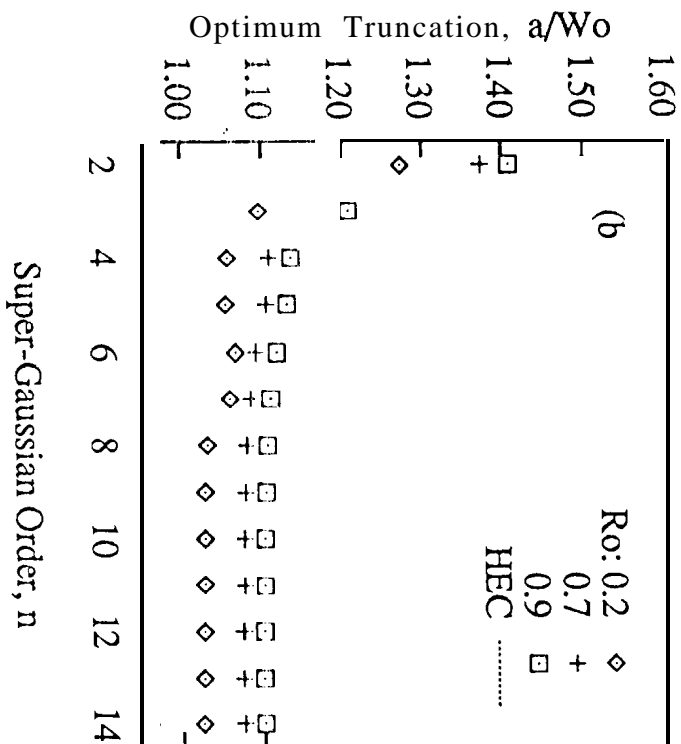
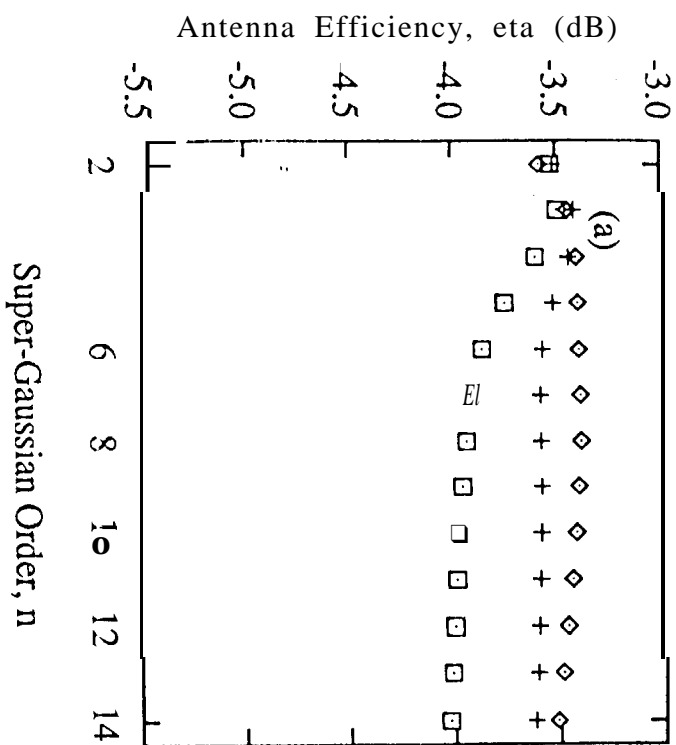


Fig. 9

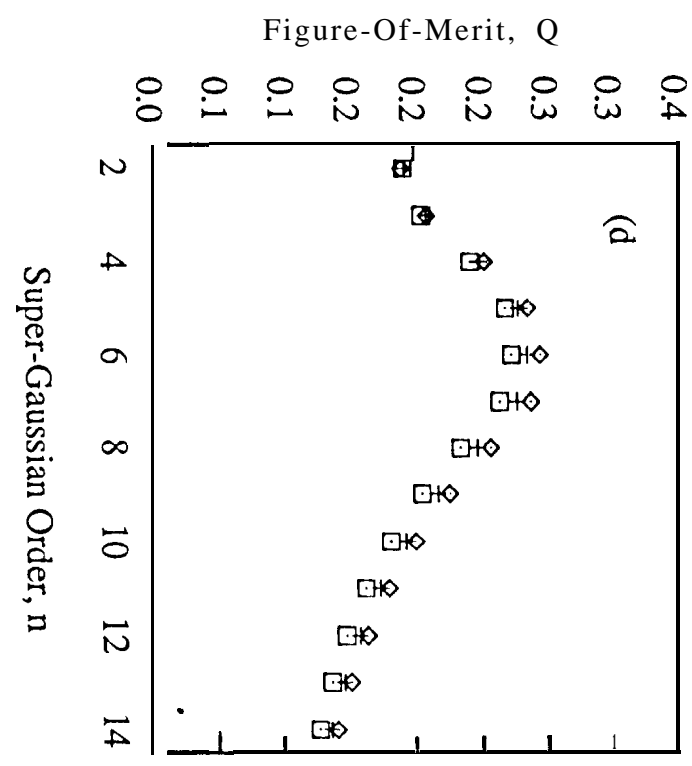
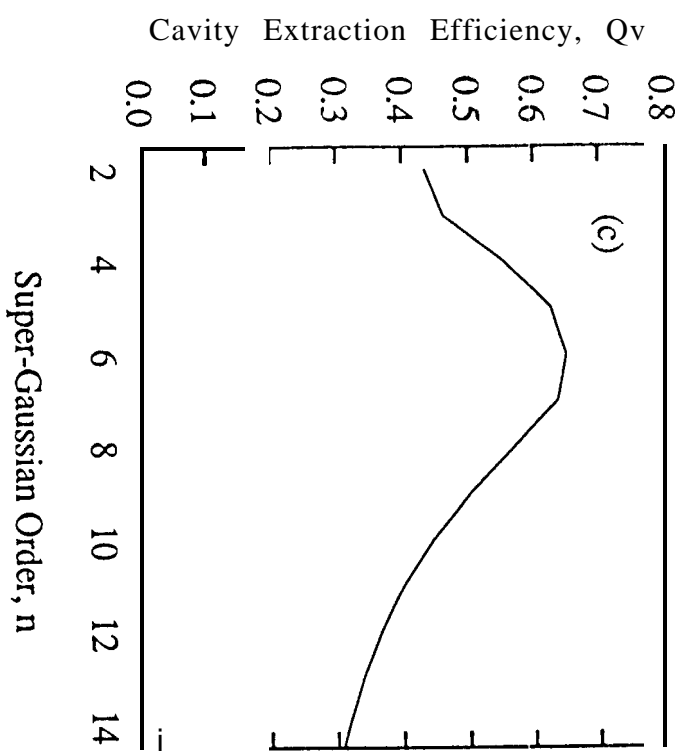
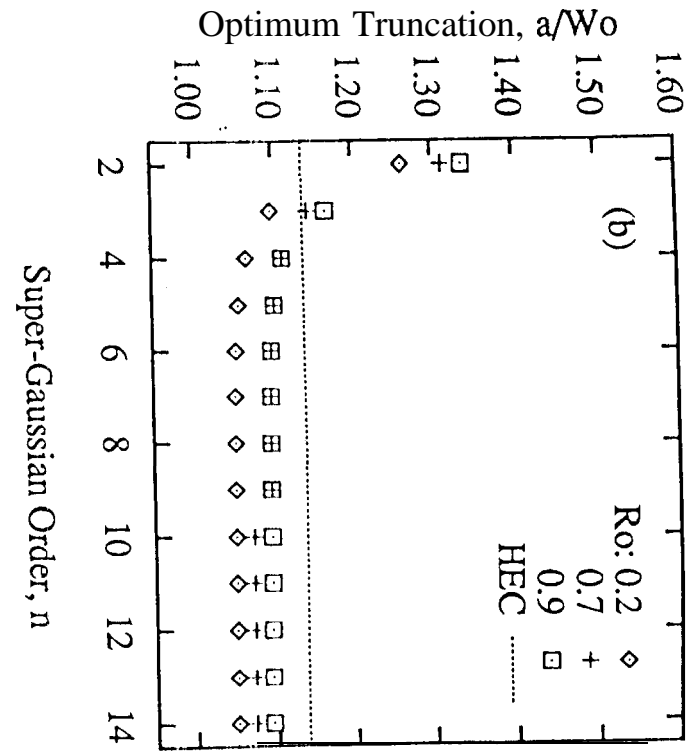
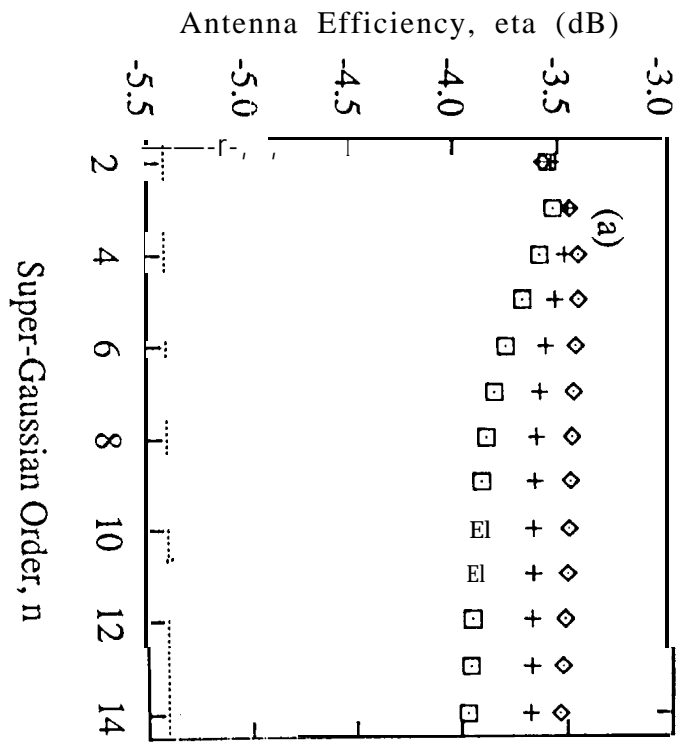


Fig. 10

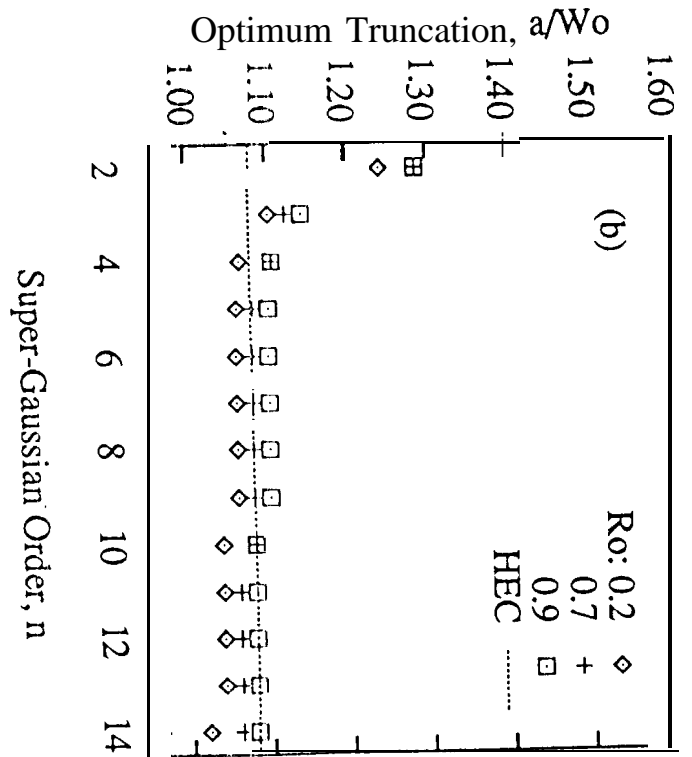
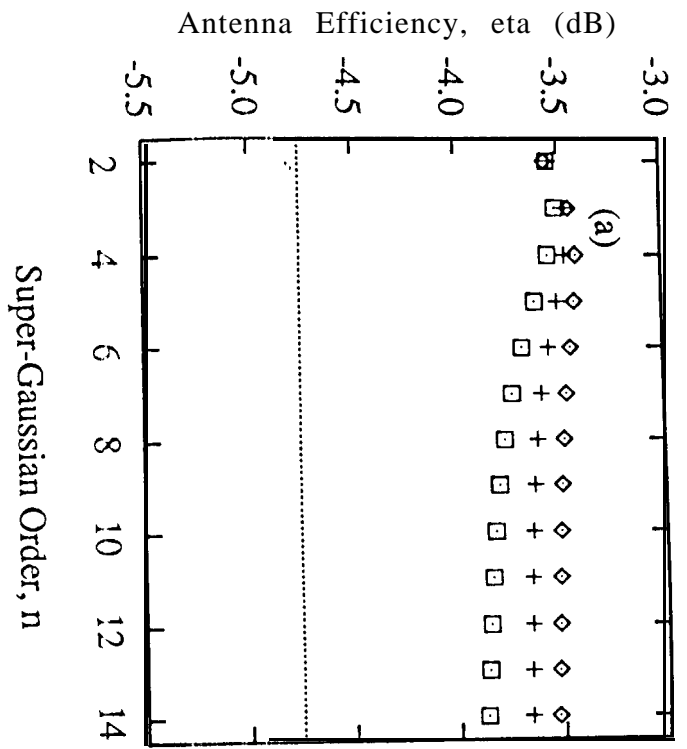
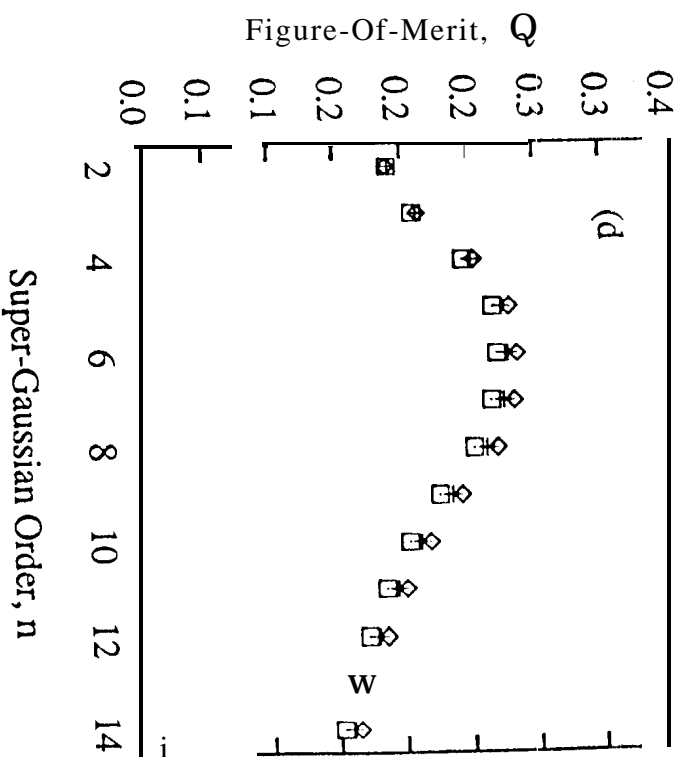
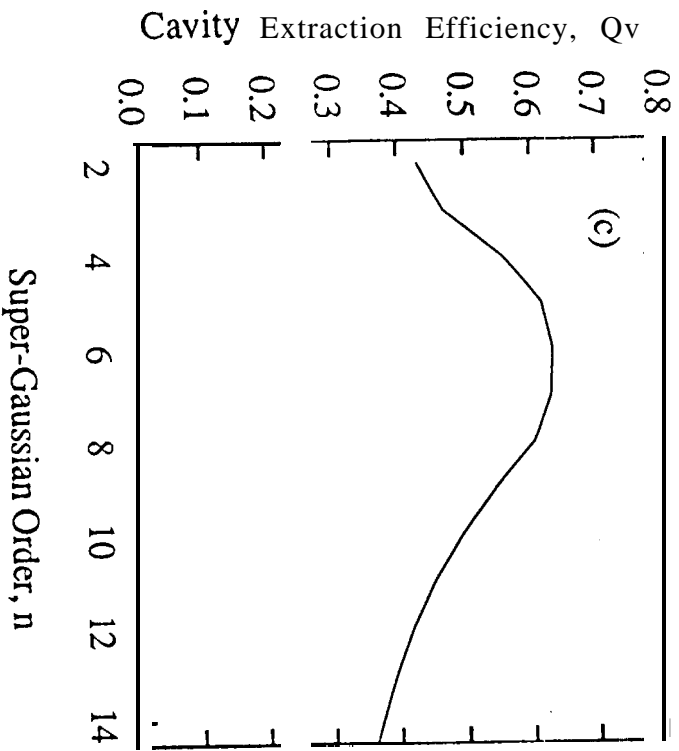


Fig. 11



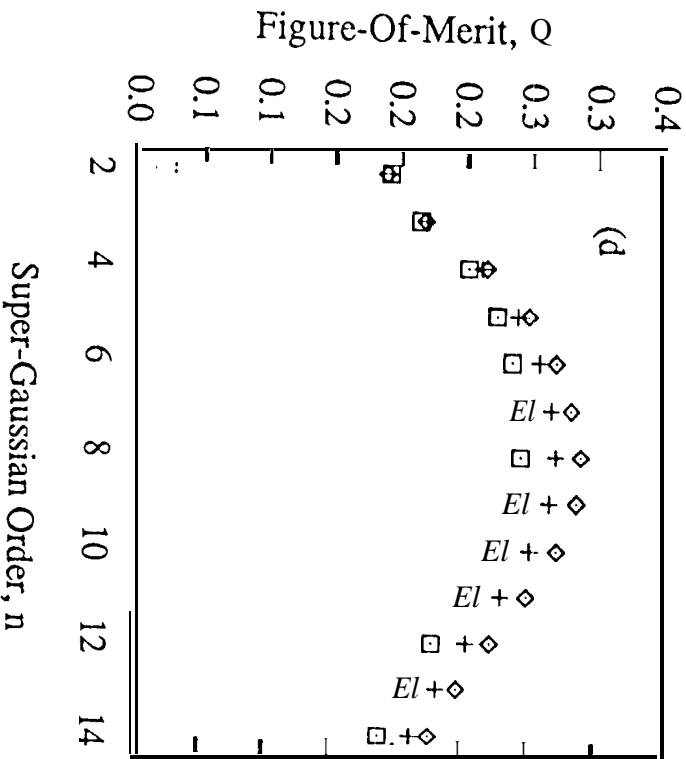
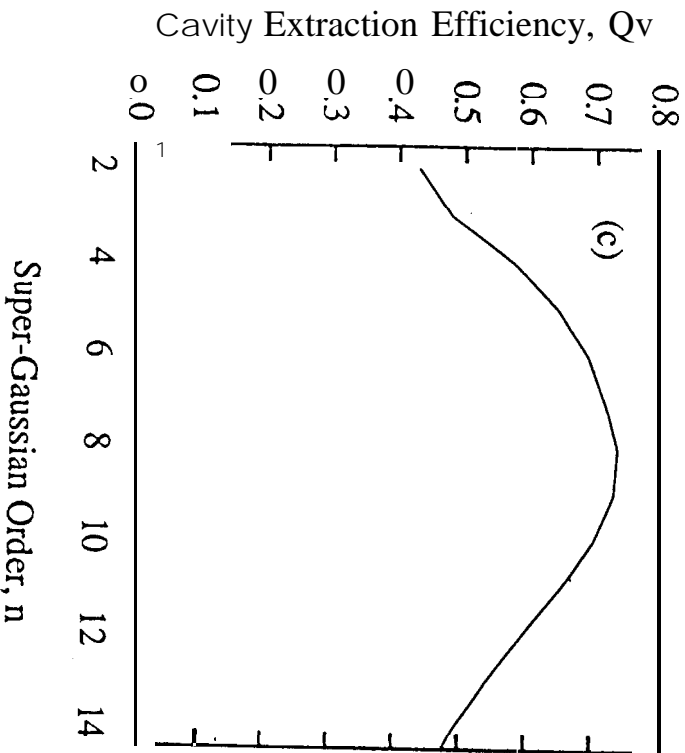
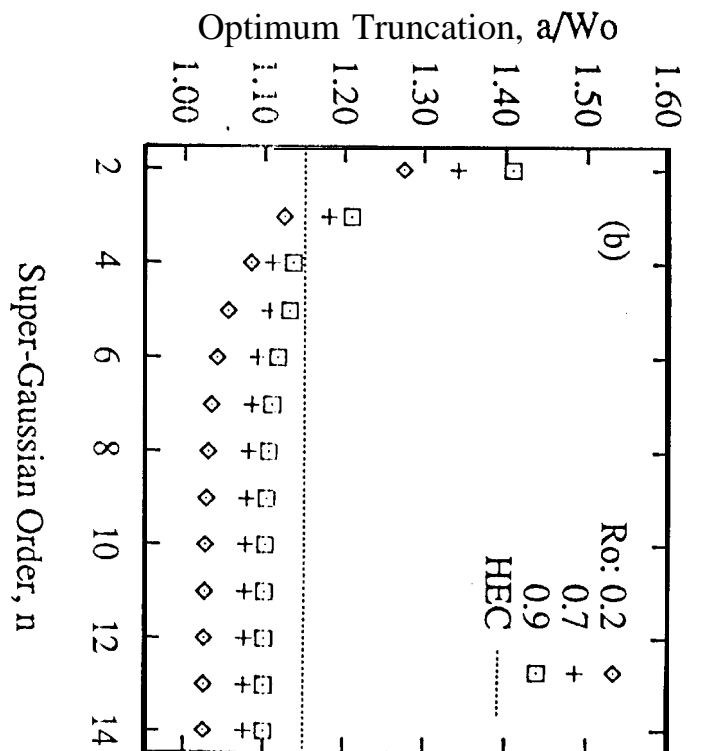
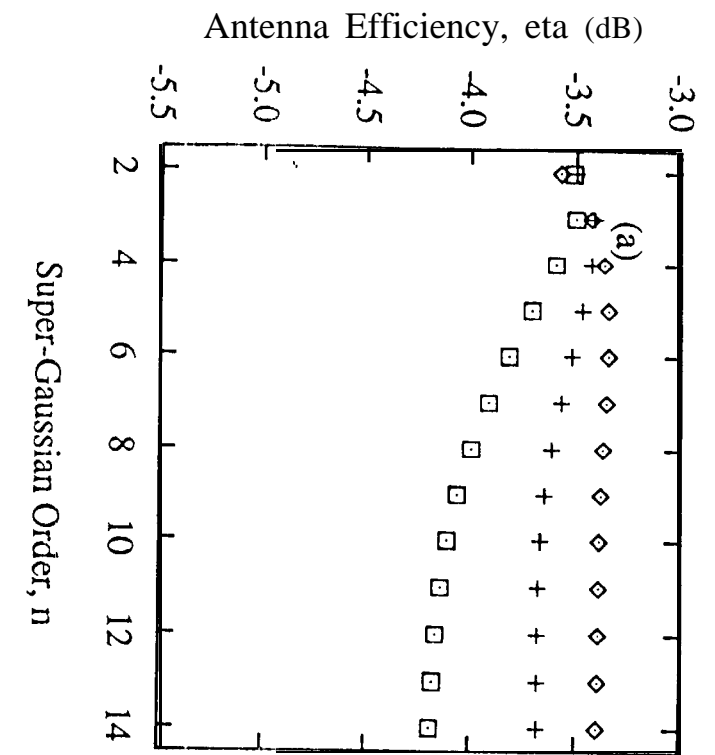


Fig. 12

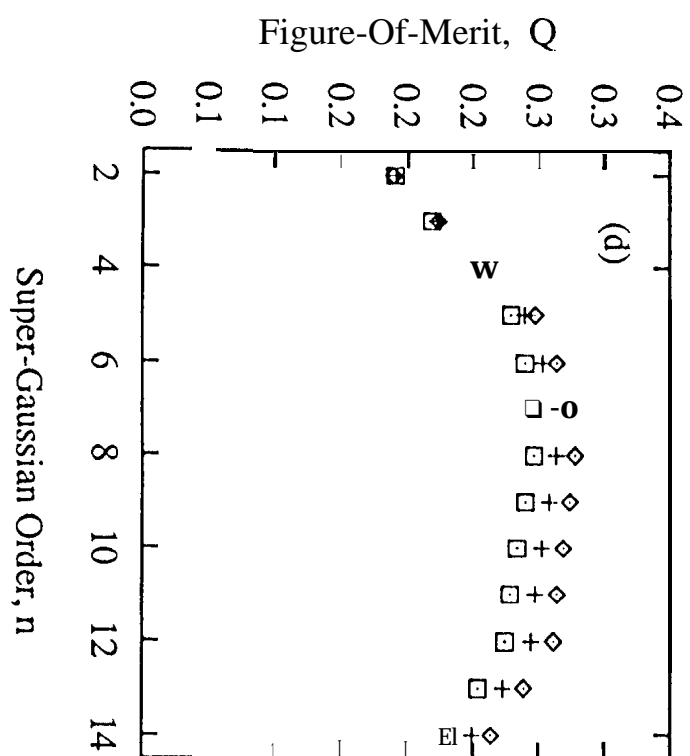
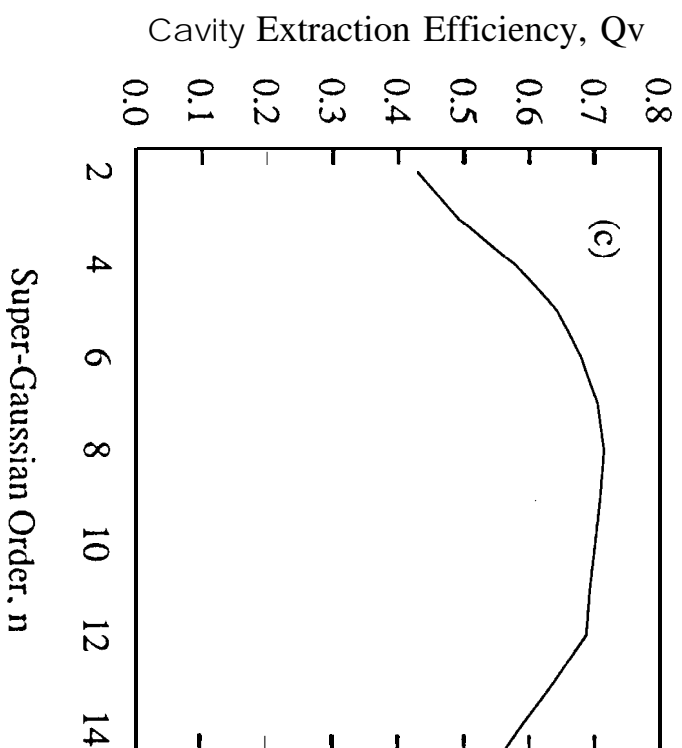
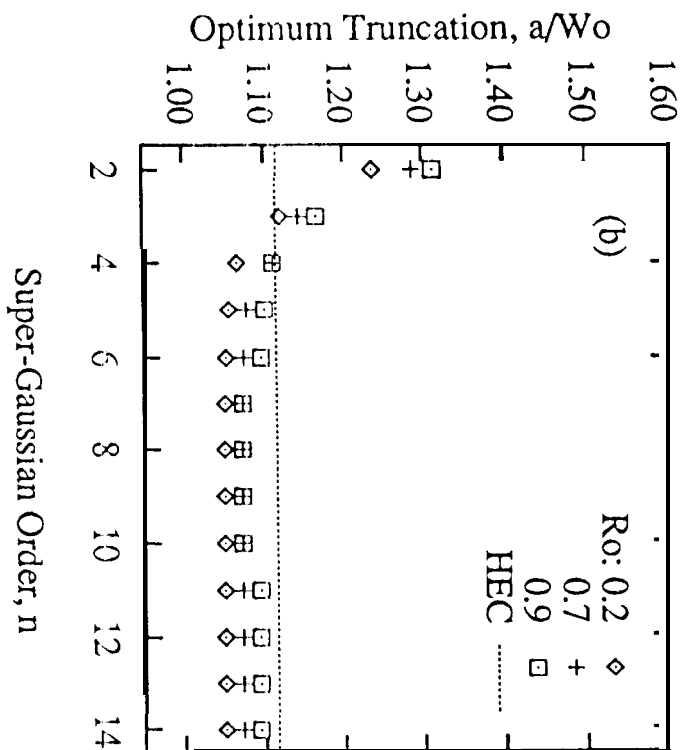
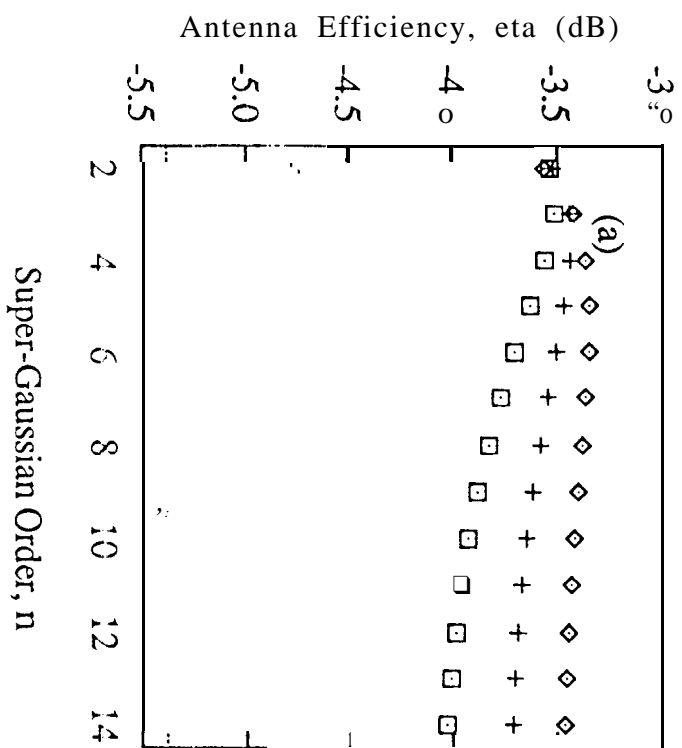


Fig.13

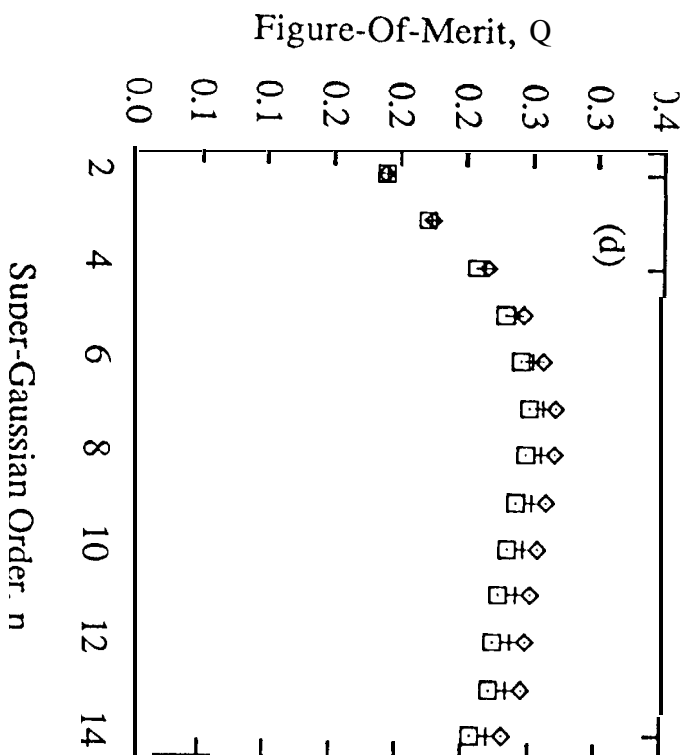
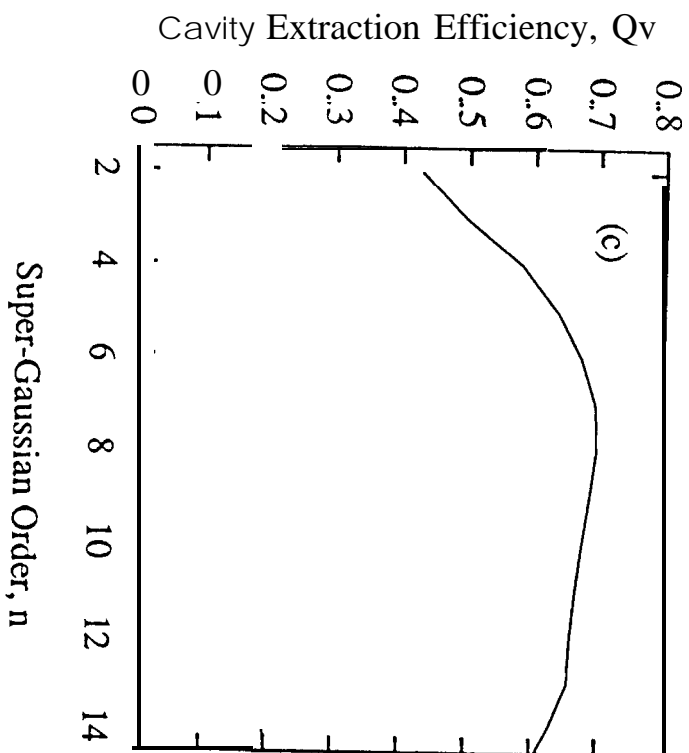
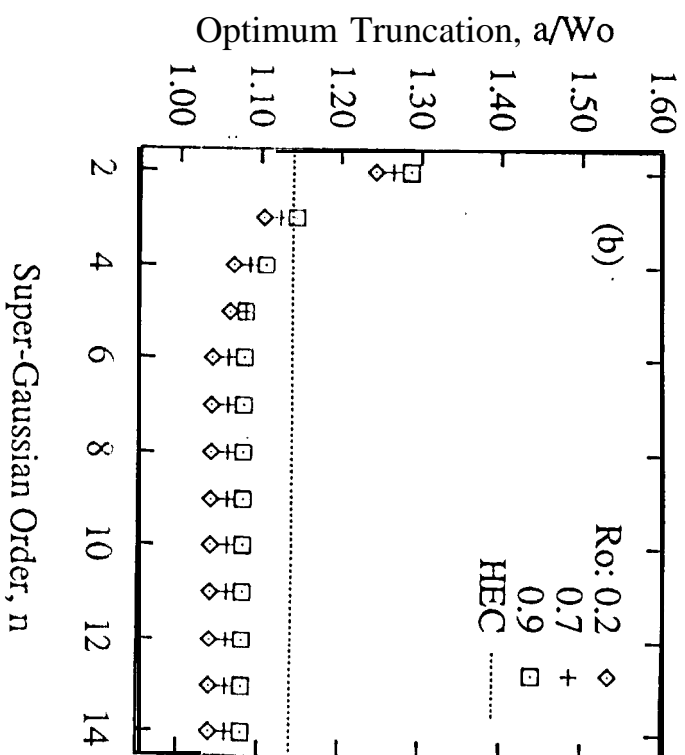
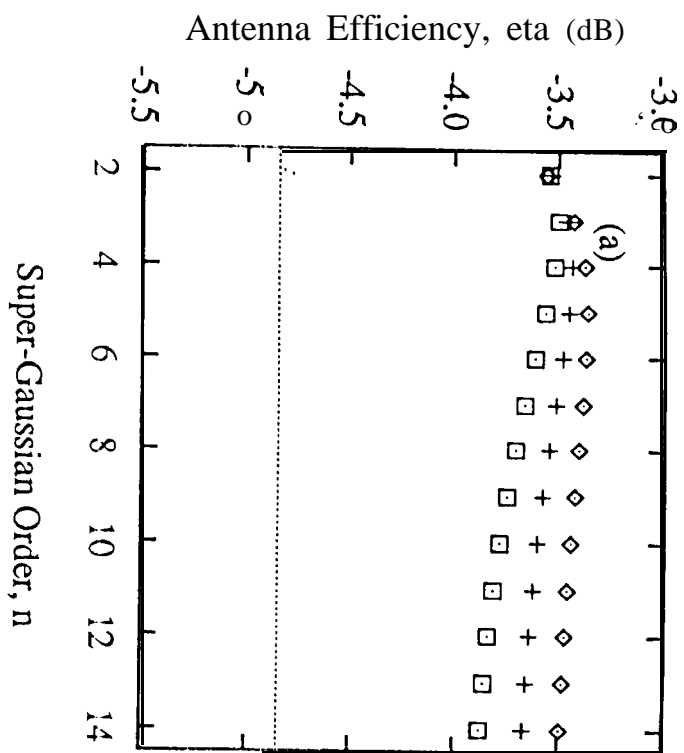


Fig. 14

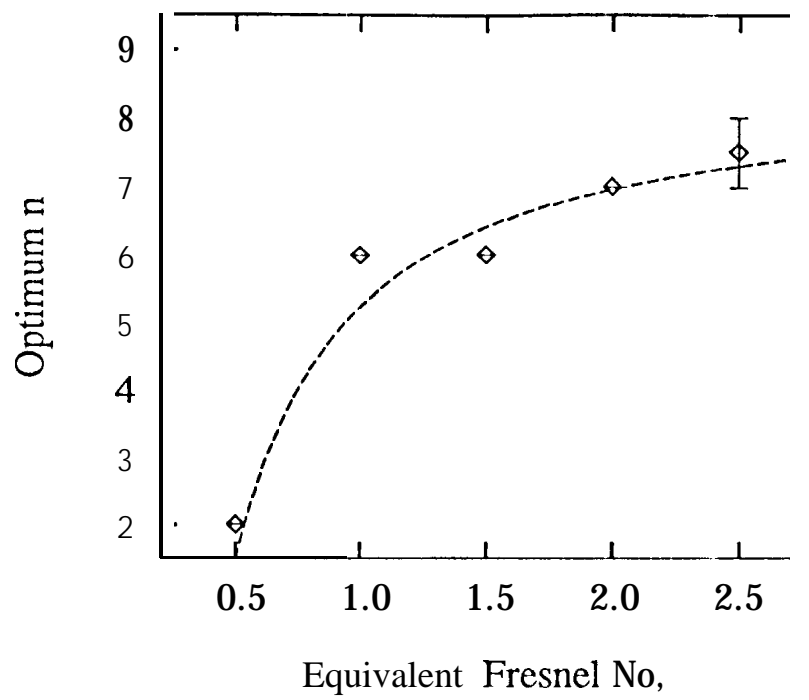


Fig. 15